International Journal of Mechanical Sciences 275 (2024) 109316

Contents lists available at ScienceDirect

International Journal of Mechanical Sciences

journal homepage: www.elsevier.com/locate/ijmecsci

Phase-field simulation and machine learning of low-field magneto-elastocaloric effect in a multiferroic composite

Wei Tang [a], Shizheng Wen [b], Huilong Hou [c], Qihua Gong [a,d,*], Min Yi [a,**], Wanlin Guo [a]

[a] State Key Laboratory of Mechanics and Control for Aerospace Structures & Key Laboratory for Intelligent Nano Materials and Devices of Ministry of Education & Institute for Frontier Science & College of Aerospace Engineering, Nanjing University of Aeronautics and Astronautics (NUAA), Nanjing 210016, China
[b] Department of Mathematics, ETH Zurich, Zürich 8092, Switzerland
[c] Key Laboratory of Aerospace Materials and Performance (Ministry of Education), School of Materials Science and Engineering, Beihang University, Beijing 100191, China
[d] College of Physics, Nanjing University of Aeronautics and Astronautics (NUAA), Nanjing 211106, China

ARTICLE INFO

Keywords:
Phase-field simulation
Machine learning
Shape memory alloy
Multiferroic composite
Magneto-elastocaloric effect
Adiabatic temperature change

ABSTRACT

Achieving appreciable elastocaloric effect under low external field is critical for solid-state cooling technology. Here, a non-isothermal Phase-Field Model (PFM) coupling martensitic transformation with mechanics, heat transfer and magnetostrictive behavior is proposed to simulate Magneto-elastoCaloric Effect (M-eCE) that is induced by magnetic field in a multiferroic composite (e.g., Magnetostrictive-Shape Memory Alloys (MEA-SMA) composite). In the PFM, a nonlinear constitutive hyperbolic tangent model is utilized to model the macroscopic magnetostrictive behavior of MEA, and the heat transfer coupled with phase transformation is employed to calculate the adiabatic temperature change (ΔT_{ad}) during M-eC cooling cycles. The influences of magnetic field, geometrical dimension, and ambient temperature on ΔT_{ad} are comprehensively investigated. Machine Learning (ML) is further conducted on the database from PFM simulations to accelerate the prediction and design of MEA-SMA composite with an improved ΔT_{ad}. It is found that a large ΔT_{ad} of 10–14 K and a wide working temperature window of 30 K can be achieved under ultra-low magnetic field of 0.15–0.38 T by optimizing the composite's geometrical dimension. The present work combining PFM and ML for evaluating M-eCE provides a theoretical framework for the optimization of M-eC cooling devices, and is also potentially extended to other multicaloric effects (e.g., electro-elastocaloric effect).

1. Introduction

Solid-state cooling techniques based on the elasto- [1–3], magneto- [4,5], and electro-caloric [6,7] effects effectively reduce the global annual emission of greenhouse gases, thus alleviating a series of negative geological effects caused by global warming [8]. Compared with traditional refrigeration techniques using environmentally harmful fluids, the environmentally friendly and efficient solid-state cooling techniques open up a magnificent prospect for the future refrigeration industry [9]. Elastocaloric cooling, exploiting the change in temperature or entropy during the stress-induced Martensite Transformation (MT) of Shape Memory Alloys (SMAs), has recently emerged as a strong solid-state cooling technology candidate due to the great adiabatic temperature change (ΔT_{ad}) compared to magneto- and electro-caloric cooling [10,11]. However, the larger required stress activating MT in elastocaloric cooling hinders its commercial application, for instance, ≥ 600 MPa for common Ni-Ti alloy [12–14], ~800 MPa for Ni_2FeGa [15], ~300 MPa for Cu-Al-Mn [16], and 320 MPa for Cu-Zn-Al [17,18]. In addition, the magnetic or electric field is handily applied to caloric materials with less heat loss, compared with the contact loading in elastocaloric devices [19]. Thus multicaloric materials and configurations integrating strengths in various solid-state cooling will have broader prospects in the much-needed compact and environmentally friendly refrigeration technologies [20,21].

In 2018, Hou et al. [22] firstly demonstrated magnetic-field manipulation of the Magneto-elastoCaloric Effect (M-eCE) in a Terfenol-D/CuAlMn composite. Different from the stress-induced eCE in metamagnetic SMAs [23], the magneto-elastocaloric cooling derives its functionalities from the rich physics of Magneto-strictive-Shape Memory Alloy (MEA-SMA) composite structure, as shown in Fig. 1. Such a composite system contains a Terfenol-D MEA cuboid, a superelastic MnCu SMA cuboid, and a frame to constrain these two. When a magnetic field is applied, the SMA cuboid is compressed owing to the

* Corresponding author.
** Corresponding author.
E-mail addresses: gongqihua@nuaa.edu.cn (Q. Gong), yimin@nuaa.edu.cn (M. Yi).

https://doi.org/10.1016/j.ijmecsci.2024.109316
Received 21 November 2023; Received in revised form 20 April 2024; Accepted 22 April 2024
Available online 27 April 2024

Nomenclature

Acronyms

ANN	Artificial Neural Network
FCC	Face-Centered Cubic
FCT	Face-Center Tetragonal
HT	Hyperbolic Tangent
M-eCE	Magneto-elastoCaloric Effect
MAE	Mean Absolute Error
MEA	Magnetostrictive Alloy
ML	Machine Learning
MT	Martensite Transformation
PCC	Pearson Correlation Coefficient
PFM	Phase-field Model
RMSE	Root Means Square Error
SMA	Shape Memory Alloy

Greek

α	Thermal conductivity
β	Gradient energy coefficient
η	Order parameter
μ	Magnetic permeability
ϕ	Magnetic potential
ρ	Density
σ	Stress
ε	Strain

Roman

A	Area
B	Magnetic induction
c	Elastic constant
ΔG	Energy barrier
ΔT	Temperature change
F	Total free energy
g	Magnetostrictive constant
H	Magnetic field intensity
L	Kinetic coefficient
l	Length
Q	Latent heat
T	Temperature

Subscripts

act	Activation
ad	Adiabatic
i	Martensite variant i
m	Martensite

Superscripts

chem	Chemical free energy
ela	Elastic strain energy
grad	Gradient energy
max	Maximum
ref	Reference
th	Thermal
tr	Transformation

magnetostrictive effect of Terfenol-D, and a temperature rise can be observed in SMA due to the release of latent heat during the forward MT. Conversely, upon the removal of the magnetic field, the force loaded on SMA is released, resulting in a temperature decrease due to the absorption of latent heat during the reverse MT. Here, magnetic field is applied instead of mechanical field to induce the MT, and thus ΔT_{ad} of SMA can be manipulated by the magnetic field in the MEA-SMA composite. M-eCE cooling combines the advantages of large ΔT_{ad} in elastocaloric cooling and low magnetic field without contact in magnetocaloric devices. Other similar state-of-the-art approaches, such as electric-field manipulation of the magnetocaloric effect in a FeRh/PZT composite [24], dual-stimulus multicaloric effect in FeRh/BTO composite [25], dual-peak phenomenon of magnetocaloric coupling in Ni/PZT/Terfenol-D composites [26], and multicaloric effect in Ni-Mn-In [27] and Ni-Mn-Ti [28], are built to explore the multicaloric effect by applying multiple field to composite materials.

However, efforts on theoretical and experimental M-eCE studies are still highly desired [20,22], which involve eCE caused by ferroelasticity in SMA and magnetostrictive behavior in MEA. To optimize the design of MEA-SMA composite system, a thermo-magneto-mechanical coupling model is important and urgently needed. In general, the eCE is simulated by either Phase-Field Model (PFM) [29–32] or thermal–mechanical phenomenological constitutive models [33–35]. The phenomenological Tanaka-type model [17,36,37], the analytical model for operating caloric devices [38], the thermo-mechanically coupled constitutive model [39], the phase transformation kinetic models [40–42], and crystal plasticity-based constitutive model [43–45] can be used to obtain the macroscopic elastocaloric properties, but have difficulties in simulating the spatial and temporal evolution of microstructure details during the MT. PFMs [46–50] utilize order parameters to describe MT, which can capture microstructure evolution, heat transfer, and stress/strain/temperature field during elastocaloric cooling. Kang et al. [51–54] conducted a comprehensive investigation into the deformation mechanism and elastocaloric effect in Ni-Ti SMA using PFM. PFM can be employed to understand the solid-state cooling mechanism and optimize for a higher ΔT_{ad}. Aiming at the magnetostrictive behavior in MEA, several nonlinear constitutive models [55–57] have been proposed. Zhan et al. [58] have successfully predicted the magneto-mechanical deformation and magnetization behaviors of MEA by means of a magneto-thermo-mechanical coupling constitutive model. On the other hand, phase-field microelasticity theory and micromagnetic approaches are also employed to model the magnetostrictive responses [59,60] in MEA and ferromagnetic domain evolution [61,62] in ferromagnetic SMA.

Up to now, the PFM to describe M-eCE in MEA-SMA multiferroic composite has not been reported yet. There is a headache involving multiscale and multiphysics including magnetics, mechanics, and thermodynamics in the simulation of M-eCE. Yu et al. [33,63–65] constructed a multiscale magneto-thermo-mechanically coupled constitutive model for calculating M-eCE, which includes a magneto-mechanically coupled constitutive model for MEA and a crystal plasticity based thermo-mechanically coupled constitutive model for SMA. Dornisch et al. [66] constructed a PFM of multiferroic heterostructures involving ferroelectric and ferromagnetic layers. The majority of these studies [33,38,39,63,64,66] have primarily focused on modeling the macroscopic-scale temperature changes of M-eCE in multiferroic composite. Describing the detailed evolutions of stress, strain, temperature, MT, and microstructure during the M-eC cooling cycle is challenging. Additionally, the tedious constitutive model with lots of fitted parameters increases the difficulty of extending the model to other systems. Herein, the PFM coupled with the nonlinear constitutive model of MEA is proposed to simulate M-eCE in MEA-SMA composite.

In addition, Machine Learning (ML) provides a significant potential to optimize and accelerate the development of magnetocaloric [67,68], electrocaloric [69] and elastocaloric effect [70–72]. For instance, Zhao

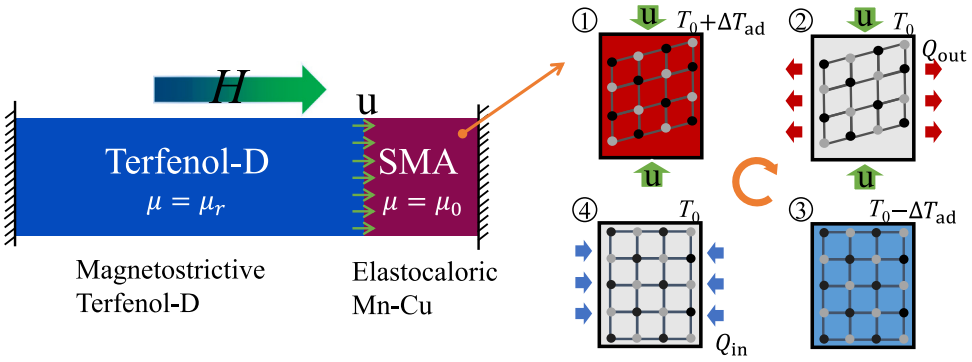

Fig. 1. Illustration of multiferroic composite and magneto-elastocaloric effect. The frame of the device acts as a fixed constraint against the overall extension of the multiferroic composite, thus transferring the mechanical load from the Terfenol-D to the SMA. Terfenol-D shows elongation when magnetic field H is applied along the length of Terfenol-D. Then, the elastocaloric Mn-Cu generates an adiabatic temperature change (ΔT_{ad}) caused by martensite transformation under a magneto-induced strain (①). This heated material then releases heat to the surroundings and cools down to the ambient temperature (②). When the stress is removed, the crystal structure transforms back to the austenitic phase (③). Finally, the material cools down and is now able to absorb heat from the surroundings (④).

et al. [70] adopted ML and theoretical calculations to discover the multi-component Cu-Al-based SMA with the highest entropy change. Similarly, by means of ML and first-principles calculations, ΔT_{ad} in NiTi-based SMA can be predicted under relevant features including volume change and lattice parameters [71]. These indicate that ML combined with other calculation methods could provide efficient avenues for predicting M-eCE and spearhead unknown caloric materials discovery.

In this work, we combine ML with PFM to accelerate the calculation and optimization of M-eCE using data obtained from PFM simulations. In detail, a non-isothermal phase-field framework coupling MT with mechanics, heat transfer, and magnetostrictive behavior is proposed to evaluate M-eCE. The evolutions of stress, strain, temperature, MT, and microstructure during the M-eC cooling cycle are captured, and the effects of magnetic field, geometric dimension, and temperature on ΔT_{ad} are revealed. Further, ML is shown to efficiently predict ΔT_{ad} of M-eCE and optimize MEA-SMA composite's geometrical dimension with a higher ΔT_{ad}. This work provides a robust theoretical framework that combines PFM and ML for designing multiferroic composite with giant M-eCE.

The paper is organized as follows. In Section 2, we present the details on PFM and ML for M-eCE, emphasizing the non-isothermal PFM that combines MT, heat transfer, and magnetostrictive behavior. We then in Section 3 carry out a series of phase-field simulations for ferroelastic behavior and M-eCE in the multiferroic composite, and utilize ML to accelerate the calculation of ΔT_{ad} and efficiently optimize the M-eCE configuration. Finally, Section 4 gives the conclusive summary.

2. Phase-field model and machine learning

In this section, we first apply a non-isothermal phase-field framework to a model M-eCE in MEA-SMA composite, utilizing MnCu as SMA and Terfenol-D as MEA. Detailed formulations for the total free energy, constitutive relations, field equilibrium equations, and evolution equations are presented. Then, ML is introduced to accelerate the optimization of ΔT_{ad} in M-eCE. In MnCu SMA, there exist a Face-Centered Cubic (FCC) high-symmetry austenitic phase at high temperature and three variants of a Face-Center Tetragonal (FCT) low-symmetry martensitic phase at low temperature [73]. The three martensitic variants are energetically equivalent. Herein we choose non-conserved order parameters η_i ($i = 1, 2, 3$) to represent the phase structures in PFM, and the value of η_i varies from 0 to 1. For Terfenol-D MEA, a nonlinear constitutive model is adopted in PFM to describe the magnetostrictive behavior.

2.1. Total free energy

In the PFM, the total free energy F of the system is driving force for microstructure evolution and consists of the chemical free energy F^{chem}, the gradient free energy F^{grad}, and the elastic strain energy F^{ela}, i.e.,

$$F = F^{chem} + F^{grad} + F^{ela}. \tag{1}$$

The chemical free energy represents the chemical driving force of the MT in a stress-free system, which can be expressed as a Landau 2-3-4 polynomial [74], i.e.,

$$F^{chem} = \int_{\Omega} \left[\frac{A}{2}(\eta_1^2+\eta_2^2+\eta_3^2) - \frac{B}{3}(\eta_1^3+\eta_2^3+\eta_3^3) + \frac{C}{4}(\eta_1^2+\eta_2^2+\eta_3^2)^2 \right] \mathrm{d}v, \tag{2}$$

where A, B and C are positive temperature-dependent coefficients, expressed as $A = 32\Delta G^*$, $B = 3A - 12\Delta G_m$ and $C = 2A - 12\Delta G_m$. ΔG^* is the temperature-dependent energy barrier between austenite and martensite. ΔG_m is the driving force of MT. Since the MT is a first-order diffusionless structural transformation and is not sharp in real materials [75], herein we formulate the energy barrier as a smooth function of temperature. Specifically, we take advantage of the hyperbolic tangent function to modify the piecewise ΔG^* function [49], i.e.,

$$\Delta G^* = \frac{0.3Q}{64}\left(1 - \tanh\left(\frac{T-T_0}{\delta T}\right)\right) + \frac{[0.8 + 0.06(T-T_0)]Q}{64}\left(1 + \tanh\left(\frac{T-T_0}{\delta T}\right)\right). \tag{3}$$

ΔG_m is also a continuous function of temperature, i.e,

$$\Delta G_m = \frac{Q(T-T_0)}{T_0}, \tag{4}$$

where Q is the specific latent heat and T_0 is the chemical equilibrium temperature. Noted that δT is a new parameter associating with the energy barrier, which could be adjusted according to the transformation temperature window from experimental results. We assume a moderately sharp transition and set $\delta T = 2$ K in this work. This modification could resolve the difficulty of calculating ΔT_{ad} by PFM at the transition point.

The gradient energy or interface energy can be expressed as

$$F^{grad} = \int_{\Omega} \frac{1}{2}\beta \left[(\nabla\eta_1)^2 + (\nabla\eta_2)^2 + (\nabla\eta_3)^2\right] \mathrm{d}v, \tag{5}$$

where β is the gradient energy coefficient related to the interfacial energy density and interface thickness, and it is assumed to be isotropic.

Table 1
Material and simulation parameters for MnCu SMA [48] and Terfenol-D MEA [55].

Parameter	Name	MnCu	Terfenol-D
c_{11}	Elastic constant	76.588 GPa	81 GPa
c_{12}	Elastic constant	14.588 GPa	38.8 GPa
c_{44}	Elastic constant	31 GPa	21 GPa
c_{66}	Elastic constant	31 GPa	38 GPa
g_{11}	Magnetostrictive constant	–	5.27×10^{-3} N/A^2
g_{12}	Magnetostrictive constant	–	3.77×10^{-4} N/A^2
g_{44}	Magnetostrictive constant	–	1.218×10^{-3} N/A^2
g_{66}	Magnetostrictive constant	–	2.204×10^{-3} N/A^2
T_0	Chemical equilibrium temperature	245 K	–
T_c	Curie temperature	–	650 K
Q	Latent heat	4.84×10^7 J/m^3	–
L	Kinetic coefficient	50 m^3/s/J	–
β	Gradient energy coefficient	2.5×10^{-9} J/m	–
α	Thermal conductivity	40 J/m/s/K	13.5 J/m/s/K
ρ	Density	7500 kg/m^3	9520 kg/m^3
c_p	Specific heat	352 J/kg/K	330 J/kg/K
μ_{11}	Magnetic permeability	–	37.5×10^{-7} N/A^2
μ_{33}	Magnetic permeability	–	37.5×10^{-7} N/A^2
μ_0	Permeability of vacuum	$4\pi\times10^{-7}$ N/A^2	$4\pi\times10^{-7}$ N/A^2

The MnCu SMA does not have magnetic-related parameters, and the parameters of Terfenol-D are determined using a strain-based hyperbolic tangent model.

The elastic strain energy contains the transformation strain $\varepsilon_{\mathrm{tr}}$ generated by structural transformation. It can be given as

$$F^{\mathrm{ela}} = \int_{\Omega} \frac{1}{2} C_{ijkl}(\varepsilon_{ij} - \varepsilon_{ij}^{\mathrm{tr}} - \varepsilon_{ij}^{\mathrm{th}})(\varepsilon_{kl} - \varepsilon_{kl}^{\mathrm{tr}} - \varepsilon_{kl}^{\mathrm{th}})\mathrm{d}v, \tag{6}$$

where C_{ijkl} is the component of the fourth-order elastic tensor, and c_{ij} in Table 1 are the elastic constants in Voigt notation, i.e. $c_{12} = C_{1122}, c_{34} = C_{3312}, c_{56} = C_{2313}$. ε_{ij} is the total strain tensor and is given by

$$\varepsilon_{ij} = \frac{1}{2}\left(\frac{\partial u_i}{\partial x_j} + \frac{\partial u_j}{\partial x_i}\right), \tag{7}$$

in which u_i is the displacement. $\varepsilon^{\mathrm{tr}}$ can be expressed as the stress-free eigen strain, which is in general defined as

$$\varepsilon_{ij}^{\mathrm{tr}} = \varepsilon_{ij}^{00}(1)\eta_1 + \varepsilon_{ij}^{00}(2)\eta_2 + \varepsilon_{ij}^{00}(3)\eta_3, \tag{8}$$

$\varepsilon^{00}(i)$ $(i = 1,2,3)$ is determined by the orientation relationship and lattice distortion between martensite and austenite with regard to the FCC-FCT MT, i.e.,

$$\begin{aligned}
\left[\varepsilon_{ij}^{00}(1)\right] &= \begin{bmatrix} \varepsilon_3 & 0 & 0 \\ 0 & \varepsilon_1 & 0 \\ 0 & 0 & \varepsilon_1 \end{bmatrix}, \quad \left[\varepsilon_{ij}^{00}(2)\right] = \begin{bmatrix} \varepsilon_1 & 0 & 0 \\ 0 & \varepsilon_3 & 0 \\ 0 & 0 & \varepsilon_1 \end{bmatrix}, \\
\left[\varepsilon_{ij}^{00}(3)\right] &= \begin{bmatrix} \varepsilon_1 & 0 & 0 \\ 0 & \varepsilon_1 & 0 \\ 0 & 0 & \varepsilon_3 \end{bmatrix},
\end{aligned} \tag{9}$$

where $\varepsilon_1 = (a - a_c)/a_c$ and $\varepsilon_3 = (c - a_c)/a_c$. As well as $\varepsilon_1 = 0.01$ and $\varepsilon_3 = -0.02$ in MnCu SMA [48].

In addition, the thermal strain is computed as

$$\varepsilon_{ij}^{\mathrm{th}} = \alpha_{ij}(T - T^{\mathrm{ref}}), \tag{10}$$

where α_{ij} is a tensor representing thermal expansion. T^{ref} is the reference temperature at which there is zero thermal strain. In the PFM simulations, T^{ref} is the initial temperature.

2.2. Nonlinear constitutive model for Terfenol-D

To model the magnetostrictive behavior in Terfenol-D MEA, a nonlinear constitutive hyperbolic tangent (HT) model is applied in this work, which can be written as [55]

$$\begin{aligned}
\sigma_{ij} &= C_{ijkl}\varepsilon_{kl} - \frac{1}{k^2} g_{ijkl}\tanh(kH_k)\tanh(kH_l) \\
B_k &= \mu_{kl}^{\varepsilon} H_l + \frac{2}{k} g_{klmn}\varepsilon_{mn}\frac{\sinh(kH_l)}{\cosh^3(kH_l)},
\end{aligned} \tag{11}$$

where B_k the magnetic induction vector, μ_{kl} the magnetic permeability, H_k the magnetic field intensity vector, and $H = -\nabla\phi$ where ϕ is the magnetic potential. k is a relaxation parameter that is adequately chosen to make the independent variable of the hyperbolic function dimensionless, and is chosen as $k = 8\times10^{-8}$ m/A. g_{ijkl} is magnetostrictive modulus tensor, and g_{ij} in Table 1 are the magnetostrictive constants in Voigt notation. The magnetostrictive behavior in Terfenol-D MEA is shown in Fig. 3(b).

2.3. Field equilibrium equations

2.3.1. Mechanical equilibrium equation

The mechanics is considered in the modeling. For the body Ω with a boundary $\partial\Omega$, the quasi-static mechanical equilibrium equation and boundary conditions are described by

$$\sigma_{ij,j} + f_i = 0 \quad \text{in } \Omega, \tag{12}$$

$$u_i = \hat{u}_i \quad \text{on } \partial\Omega_u, \quad \sigma_{ij}n_j = \hat{t}_i \quad \text{on } \partial\Omega_\sigma, \tag{13}$$

where σ_{ij} is the Cauchy stress and f_i is the body force, and we assume $f_i = 0$. $\hat{u}$ and $\hat{t}$ are the displacement and surface traction on the boundary part $\partial\Omega_u$ and $\partial\Omega_\sigma$, respectively.

2.3.2. Force balance for multiferroic composite

For the contact mechanics, force balance for the multiferroic MEA-SMA system should be always satisfied, and the force balance can be simplified as

$$A_1E_1\varepsilon_1 = A_2E_2\varepsilon_2, \tag{14}$$

where A_1, E_1, ε_1 and A_2, E_2, ε_2 represent cross-sectional area, elasticity constant, and strain for Terfenol-D and SMA, respectively. Under a magnetic field, the displacement without constraint of Terfenol-D is λl_1, in which l_1 is the length of Terfenol-D, and λ is magnetostrictive strain. Assuming a real displacement Δl_2 in SMA, the strain for Terfenol-D and SMA is

$$\varepsilon_1 = \frac{l_1\lambda - \Delta l_2}{l_1}, \quad \varepsilon_2 = \frac{\Delta l_2}{l_2}. \tag{15}$$

Substituting Eq. (15) into Eq. (14), the real strain or magneto-induced strain ε_2 for SMA as

$$\varepsilon_2 = \frac{\lambda}{A_2E_2/(A_1E_1) + l_2/l_1}. \tag{16}$$

Then, we nondimensionalize the area with $A^* = A_1/A_2$, and length with $l^* = l_1/l_2$ to investigate the effect of geometric dimension on M-eCE, seeing Section 3.2.3 for details.

2.3.3. Magnetic equilibrium equation

The Maxwell equation which governs the magnetic part and the magnetic boundary conditions have the form

$$B_{i,i} = 0 \quad \text{in } \Omega \tag{17}$$

$$B_i n_i = \hat{B} \quad \text{on } \partial\Omega_B, \quad \phi = \hat{\phi} \quad \text{on } \partial\Omega_\phi, \tag{18}$$

where $\hat{B}$ is the prescribed value and $\hat{\phi}$ is the given potential on the boundary part $\partial\Omega_B$ and $\partial\Omega_\phi$, respectively.

2.4. Evolution equations

Here, time-dependent Ginzburg–Landau kinetic equation [76] is used to govern the spatial and temporal evolution of η_i, i.e.,

$$\dot{\eta}_i = -L\frac{\delta F}{\delta \eta_i}, \tag{19}$$

where L is the kinetic coefficient characterizing the interfacial migration and F is the total free energy of the system.

Further, we can obtain directly ΔT_{ad} during loading and unloading by the non-isothermal PFM simulations. The temperature evolution equation can be derived as

$$\rho c\frac{\partial T}{\partial t} = \alpha\nabla^2 T + Q(\dot{\eta}_1 + \dot{\eta}_2 + \dot{\eta}_3), \tag{20}$$

where ρ, c and α are density, specific heat and the thermal conductivity of the material, respectively. Q is the latent heat and plays a critical role in temperature change during MT.

2.5. Machine learning methods

To accelerate the calculation of ΔT_{ad} and efficiently find the M-eCE configuration with the highest ΔT_{ad} value, Artificial Neural Network (ANN) based on the phase-field database is adopted. Genetic algorithms, an important category of ML techniques that achieve the goal of optimization [77,78], are chosen to improve M-eCE in this work. As shown in Fig. 2, the time-saving ML replaces time-consuming PFM simulations to calculate M-eCE by means of database obtained from PFM simulations, thus accelerating the calculation and optimization of the M-eCE system. ANN is a directed acyclic graph consisting of an input layer, several hidden layers, and an output layer. By training the model with a set number of data, it can construct a functional model from an m-dimensional input feature vector α to a corresponding one-dimensional output feature vector Q_{ANN}. The calculation process for every neuron is to take a weighted sum of its inputs x_1, x_2, x_3... x_p, send that weighted sum through an activation function, and output the final result y. The mathematically expression for kth neuron in the lth layer is calculated as [79]:

$$y = f_{act}\left(\sum_{i=1}^{p} w_i^{l,k} x_i^{l,k} + b^{l,k}\right), \tag{21}$$

where w is weight, b is bias, f_{act} is activation function. i is the index of input, x is the input vector to the $(l,\ k)$ neuron, and p represents the number of inputs to the neuron. $p = 4$ and y is ΔT_{ad} is this work, as shown in Fig. 2.

In the multilayer perceptron, 70% of data is used for training dataset, 20% for test dataset, and 10% for verification dataset. The Levenberg–Marquardt method is chosen as the train function. In detail, the target is ΔT_{ad} in output layer, and the input layer has four inputs corresponding to four characteristics: the applied magnetic field, length ratio and area ratio of MEA-SMA device, and ambient temperature.

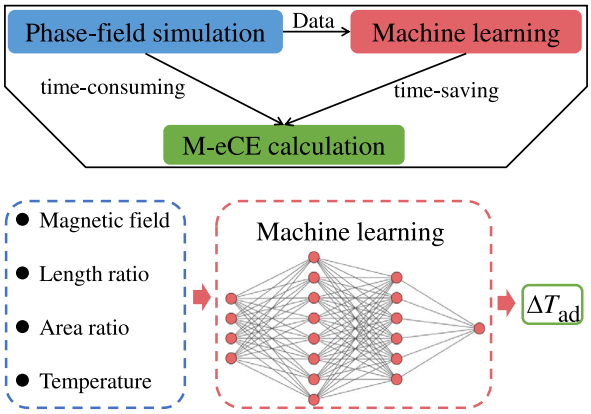

Fig. 2. Schematic illustrating the relationships among phase-field simulation, machine learning, and M-eCE calculation. Machine learning based on the database of phase-field results is adopted to accelerate the M-eCE calculation. The artificial neural network consists of four inputs (magnetic field, length ratio, area ratio and temperature) and one output (ΔT_{ad}).

3. Results and discussion

In phase-field simulations, we utilize a three-dimensional domain to model the M-eCE in the multiferroic MEA-SMA composite. The diagram of this multiferroic composite system is shown in Fig. 1. The magneto-induced strain advances the MT in SMA, thus achieving M-eCE. Both ends of the composite are constrained, with a parallel magnetic field applied along the length of Terfenol-D, and other boundaries are free in PFM simulations. The prediction capability of the proposed PFM is firstly verified by simulating the superelasticity of SMA, magnetostrictive behavior of MEA, and M-eCE in MEA-SMA composite. Then, the influences of magnetic field, geometric dimension, and temperature on ΔT_{ad} are investigated. A set of database from PFM simulations is trained using ML to predict and optimize ΔT_{ad} of M-eCE.

In addition, the finite element mesh size should be smaller than the minimum value of interface thickness ($\delta = \sqrt{\beta/2\Delta G^*} \approx 14.8$ nm) between austenite and martensite, thus the mesh size is chosen as $\Delta l = 10$ nm. The material and simulation parameters of MnCu [48] and Terfenol-D [55] used for PFM simulations are summarized in Table 1. The above PFMs are numerically implemented by finite element method in the open source Multiphysics Object Oriented Simulation Environment (MOOSE) [81], and see Appendix for details.

3.1. Ferroelastic behavior

MT would occur in MnCu SMA under external fields and leads to extraordinary macroscopic behaviors, e.g., the shape memory effect and superelasticity [48]. In order to validate the model, benchmark simulations including that stress-induced MT of SMA and magnetostrictive behavior of Terfenol-D are carried out. These phenomena are essential for inducing the M-eCE in MEA-SMA multiferroic devices.

Fig. 3(a) shows the compression-unloading stress–strain response of MnCu SMA under 270 K. Fig. 3(b) shows the magnetic field-magnetostriction strain curve of the Terfenol-D. The superelasticity effect during stress-induced MT is also clearly presented in MnCu SMA. Upon stress loading, the small martensitic embryo (red stripes for $\eta = 1$) grows to be a large martensitic domain due to the stress-induced MT. Upon unloading, the austenitic embryo (blue stripes for $\eta = 0$) grows, restoring the original state. A homogeneous temperature increment also takes place at the same area where the local strain accumulation and MT is observed in phase-field simulation, which is consistent with the experiment in CuZnAl SMA [15]. Furthermore, the simulation results for magnetostrictive behavior of Terfenol-D agree well with the experimental findings [22].

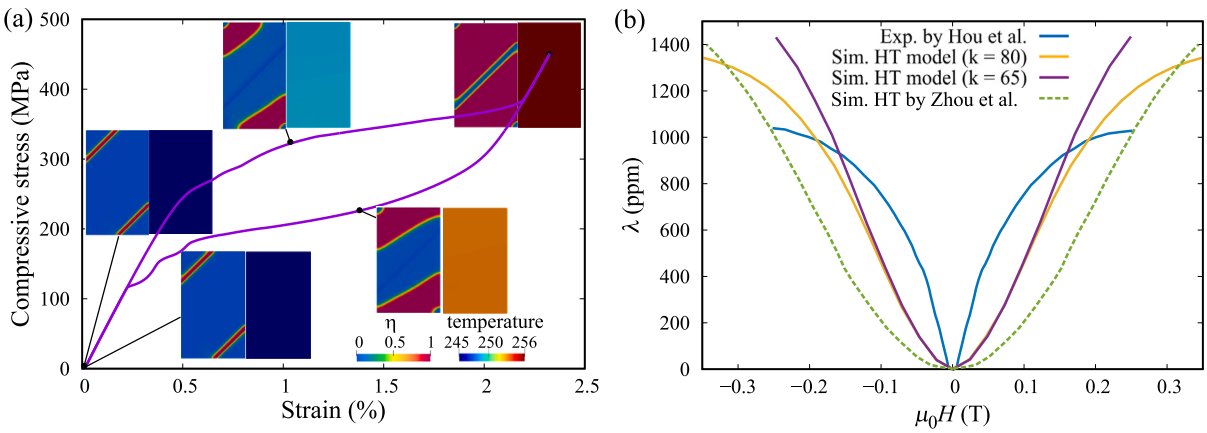

Fig. 3. Phase-field results of (a) stress–strain behavior of Mn-Cu SMA and (b) magnetostrictive behavior of Terfenol-D MEA based on nonlinear constitutive hyperbolic tangent model [80]. The martensite transformation occurs during the loading, accompanied by temperature change. The martensite and austenite phase are shown in red and blue, respectively.

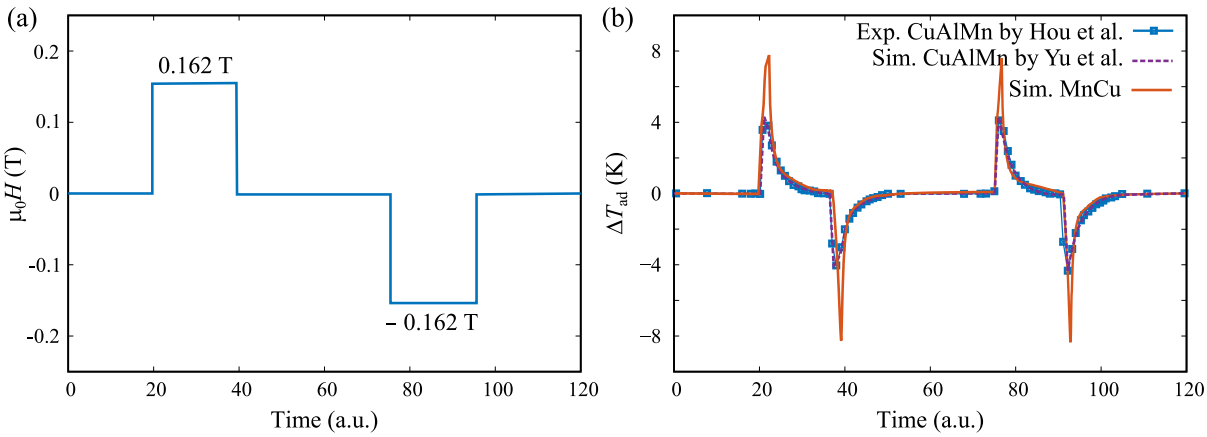

Fig. 4. Experimental and predicted result of magneto-elastocaloric effect in the MEA-SMA composite system: (a) waveform of applied magnetic field; (b) evolution of the overall temperature change of SMA. The blue dotted and dashed lines represent the experimental [22] and simulated [33] results of CuAlMn M-eCE, respectively. The orange solid line shows the temperature change of MnCu during the waveform of applied magnetic field.

3.2. Magneto-elastocaloric effect

For the integrity of the content, the experimental observations done by Hou et al. [22] and phase-field simulations for the ultra-low-field induced M-eCE of the MEA-SMA composite system are presented here. Parameters such as ΔT_{ad}, the magnetic-field-induced cooling strength $\Delta T_{ad}/\mu_0 \Delta H$ (K T^{-1}), and the working temperature window are critical for characterizing the refrigeration capacity of M-eCE materials and devices. These parameters are computed and discussed below. The Terfenol-D cuboid with the dimensions of 200 nm × 50 nm × 650 nm and the MnCu SMA specimen cuboid with the dimensions of 100 nm × 10 nm × 50 nm are used in the phase-field simulation. The applied magnetic field is 0.162 T as used in Hou et al. [22].

Fig. 4(a) depicts the waveform of applied magnetic field for the composite system. The magnetic field is initially loaded to its maximum value in a short period, and then remains unchanged for a while. After that, the magnetic field is fully unloaded. Fig. 4(b) shows the evolution of the overall ΔT_{ad} for MnCu SMA in the composite system, owing to the elastocaloric effect. The PFM effectively captures the ΔT_{ad} rise or drop of the SMA cuboid within the multiferroic composite system during the rapid application and removal of the magnetic field, and the phase-field predicted results are consistent with the semi-analytical and numerical models [33,63] and the experimental ones [22]. ΔT_{ad} as large as 8 K and $\Delta T_{ad}/\mu_0 \Delta H = 49.3$ KT^{-1} are realized in this MnCu/Terfenol-D composite.

3.2.1. Magneto-elastocaloric cooling cycle

Fig. 1 shows the frame of the M-eCE device. The mechanical strain originated from the magnetostrictive response of Terfenol-D would be transferred to SMA, thus generating eCE in SMA (the right side of Fig. 1). The SMA is subjected to a MT from FCC austenite into FCT martensite, which releases latent heat and increases ΔT_{ad} (① in Fig. 1). This heated material then releases heat to the surroundings and restores to the original temperature (②). When the applied magnetic field is removed, the crystal structure transforms back to the austenitic phase and the temperature decreases owing to the inverse MT (③). Finally, the SMA becomes a heat sink and achieves MeC cooling (④). The detailed example of M-eCE is shown in Fig. 5. The magnetic field is applied along the z-direction, and the loading history is shown as red line in Fig. 5a. Four stages including loading, holding (heating), unloading, and holding (cooling) are involved according to the loading history.

During loading and unloading, the applied magnetic field is rapidly increased to 0.19 T in Terfenol-D, and no heat flux is set to keep adiabatic condition of this system, similar to the swift loading/unloading in the experiment. The relationship between strain in SMA and the applied magnetic field is shown in Fig. 5(b), which is similar to the stress–strain curve under elastocaloric cooling and exhibits a hysteresis [49]. Note that the strain is fully recoverable, which is beneficial for fatigue performance of the MEA-SMA composite. Meanwhile, the evolutions of order parameter η_3, temperature, and stress σ_3 in SMA, from ① to ⑤ during a M-eCE cooling cycle, are shown in Fig. 5c.

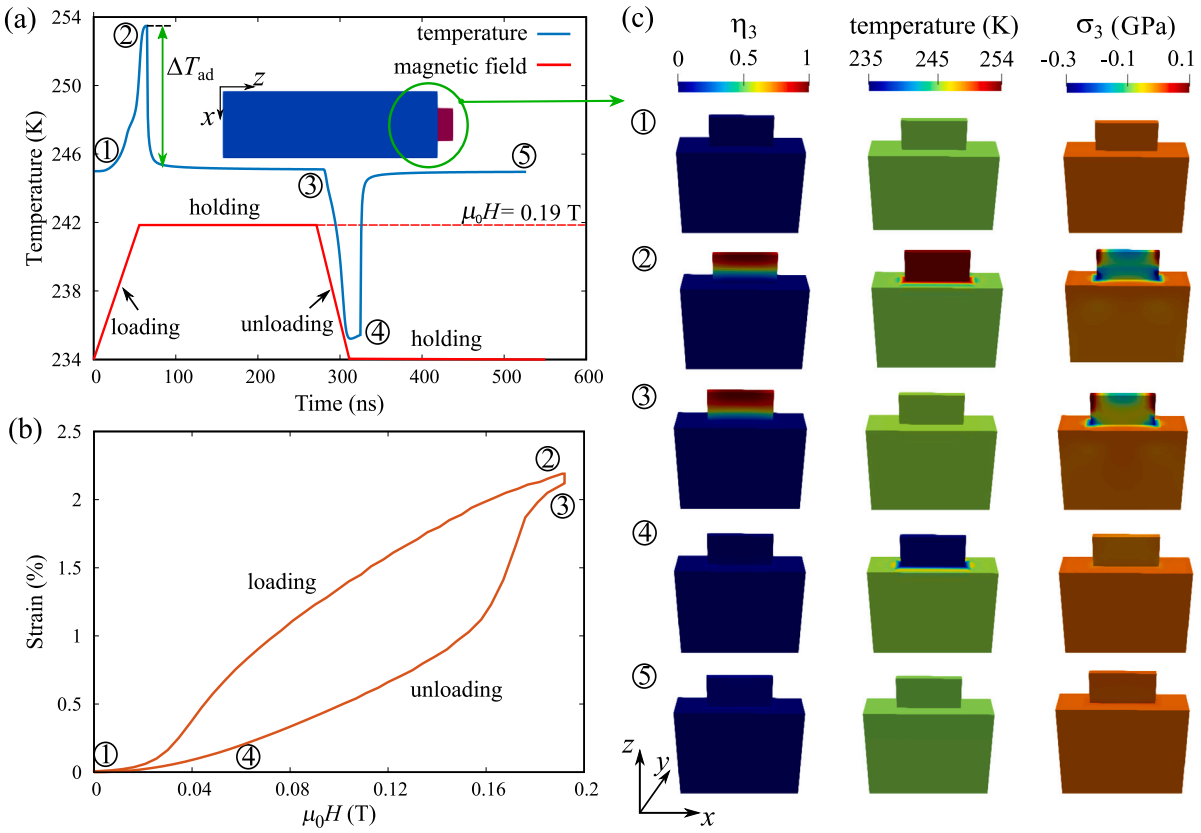

Fig. 5. (a) Adiabatic temperature change (ΔT_{ad}) in SMA under a low magnetic field ($\mu_0 H$ = 0.19 T). (b) Strain in SMA *vs.* the applied magnetic field $\mu_0 H$ in Terfenol-D. (c) Evolutions of microstructure (η_3), temperature, and stress fields during the magneto-elastocaloric (MeC) cooling cycle. The size is 200 nm × 50 nm × 650 nm for Terfenol-D and 100 nm × 10 nm × 50 nm for SMA. The ambient temperature is 245 K. ① to ② represents the loading step, ② to ③ represents the holding step, ③ to ④ represents the unloading step, and ④ to ⑤ represents the holding step during the magneto-caloric cooling cycle.

During the loading, form ① to ②, exothermic austenite–martensite transformation occurs in SMA and η_3 increases from 0 to 1. The corresponding temperature rises rapidly from 245 K to approximately 253.4 K, with a heating ΔT_{ad} = 8.4 K obtained under a low magnetic field of 0.19 T. σ_3 increases with the magnetic field due to the force balance. During holding, from ② to ③, the magnetic field is stationary, the martensitic variant 3 remains but the temperature decreases due to the heat transfer to the surroundings. During unloading, form ③ to ④, the endothermic martensite–austenite transformation cause the decreases of temperature (a cooling ΔT_{ad}) and stress. During holding, form ④ to ⑤, hypothermal SMA absorbs the external heat, all are back to the original state, and then prepare for the next cooling cycle. These simulation results on M-eCE and microstructure evolution indicate that M-eCE can be soundly handled by the non-isothermal PFM. It should also be noted that the tensile stress is very low (100 MPa) to facilitate the fatigue performance, and the maximum compressive stress (300 MPa) is smaller than the compressive strength of SMA.

3.2.2. Impact of magnetic field

Similar to the mechanical loading in eCE [16], the magnetic-field loading in M-eCE demonstrates a positive influence on ΔT_{ad}. A magnetic-field-dependent cooling strength is observed in Fig. 6, in which the evolutions of strain and temperature of SMA during MeC cooling cycle are captured. The applied magnetic field of 0.154 and 0.288 T results in a cooling ΔT_{ad} (close to heating ΔT_{ad}) of 10.8 and 12.4 K, respectively. The strain–temperature behavior during a MeC cooling cycle, as shown in Fig. 6b, reflects a recoverable transformation strain ε_{tr} and ΔT_{ad} during loading and unloading. ΔT_{ad} and ε_{tr} increase with increasing magnitude of magnetic field, showing that the magneto-induced strain in Terfenol-D is the driving force for MT in SMA. Note that ε_{tr} under $\mu_0 H$ = 0.154 T is higher than the critical transformation strain (0.02) in MnCu SMA [48]. There is a critical magnetic field that triggers the transformation strain in SMA, which can induce M-eCE in the MEA-SMA composite system. Besides, a satisfactory ΔT_{ad} of 10.8 K is calculated under an ultra-low magnetic field of $\mu_0 H$ = 0.154 T, offering theoretical guidance for low-field driven caloric effect in multiferroic composites.

3.2.3. Impact of geometric dimension

It is known that the refrigerating capacity of the composite system is proportional to the volume of MnCu SMA. Further investigation is required to explore the impact of configuration size on the refrigeration performance in MEA-SMA composites [22]. Here, the volume size of MnCu is constant and we change the Terfenol-D size to evaluate the impact of the geometric dimension. Compared with configuration between 200 × 50 × 650 and 400 × 50 × 650 nm^3 (Figs. 5(a) and 6(a)), a comparable gap in ΔT_{ad} (8.4 K for the former and 11.5 K for the latter) is observed under a same magnetic field of 0.19 T. This is attributed to that the larger magneto-induced strain generates a greater ΔT_{ad} in the bigger Terfenol-D cuboid.

Moreover, the magneto-induced strain in SMA can be briefly expressed in Eq. (16), and it is dependent on the stiffness, length and cross-sectional area ratios of the Terfenol-D MEA and MnCu SMA. The stiffness ratio of Terfenol-D and MnCu is constant. The unfavorable length ratios and cross-sectional area ratios of Terfenol-D and MnCu (proportional to strain, on the order of 10^{-2}, required to actuate the latter, but inversely proportional to magnetostriction of the former, on the order of 10^{-3}) are major weaknesses of this strategy. Therefore,

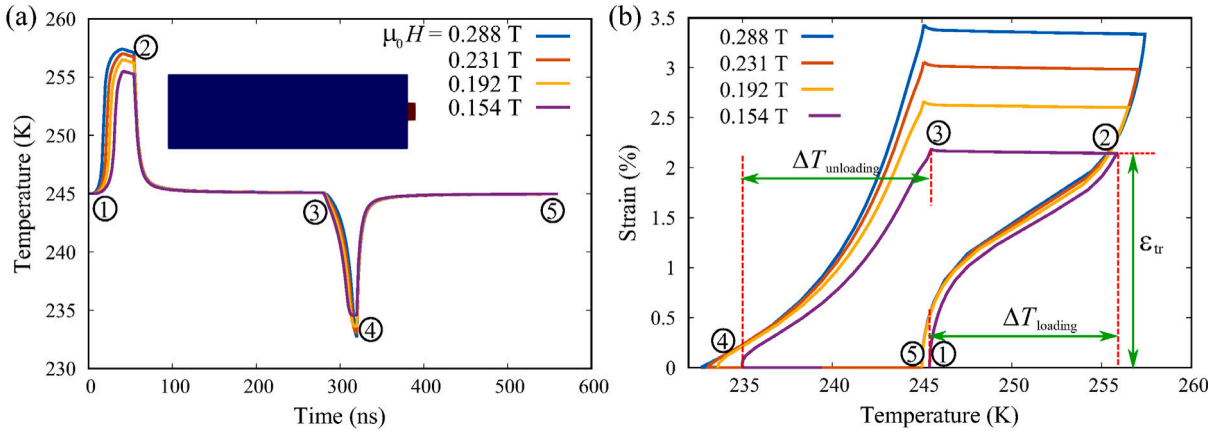

Fig. 6. (a) Temperature evolution of SMA under various magnetic fields with $\mu_0 H = 0.154$, 0.192, 0.231, 0.288 T. (b) strain–temperature curves of SMA under various magnetic fields. The size is 400 nm × 100 nm × 1300 nm for Terfenol-D and 100 nm × 10 nm × 50 nm for SMA. $\Delta T_{\text{loading}}$ and $\Delta T_{\text{unloading}}$ are the adiabatic temperature change during loading (from ① to ②) and unloading (from ③ to ④), respectively. A large magnetic field induces a large transformation strain, resulting in increased temperature change.

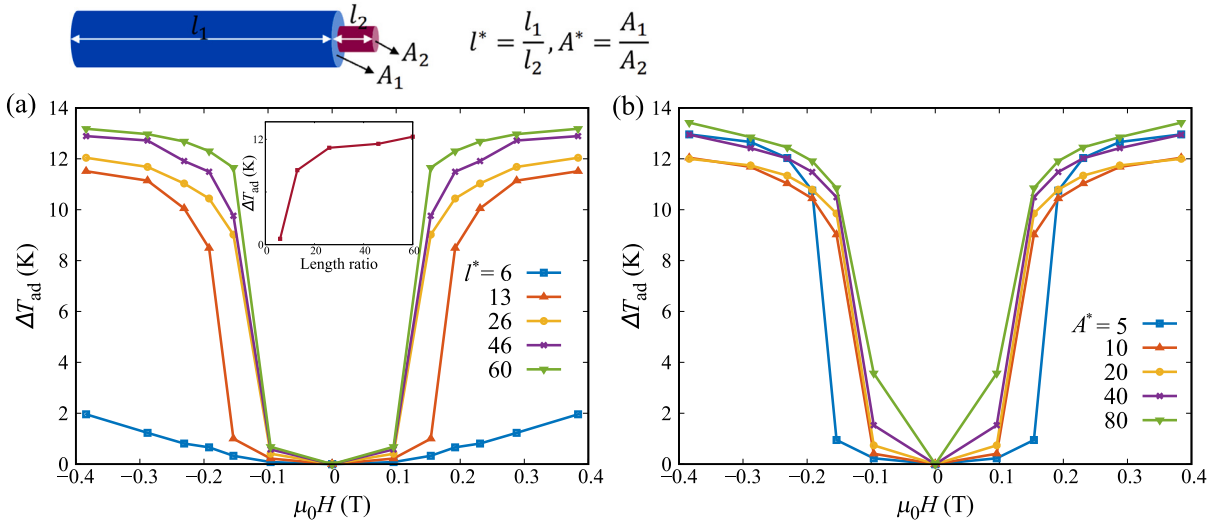

Fig. 7. The magnetic-field-dependent M-eCE with (a) $l^* = 6$, 13, 26, 46, 60 for $A^* = 10$ and (b) $A^* = 5$, 10, 20, 40, 80 for $l^* = 26$ at an ambient temperature of 245 K. Blue and red cylinders represent the Terfonel-D and SMA. The length ratio is $l^* = l_1/l_2 = l_{\text{T-D}}/l_{\text{SMA}}$ and cross-sectional area ratio is $A^* = A_1/A_2 = A_{\text{T-D}}/A_{\text{SMA}}$.

improving the ΔT_{ad} by controlling the length and cross-sectional area ratios of Terfenol-D and MnCu is necessary. Here, the size of SMA is fixed with 100 nm × 10 nm × 50 nm, and $l^* = l_1/l_2 = l_{\text{T-D}}/l_{\text{SMA}} = 6$, 13, 26, 46, 60, and $A^* = A_1/A_2 = 5$, 10, 20, 40, 80 are chosen to calculate the impact of geometrical dimension on M-eCE, as shown in Fig. 7.

Fig. 7a shows ΔT_{ad} varying with the applied magnetic field $\mu_0 H$ under various length ratios. It is observed that ΔT_{ad} changes non-monotonically with the increase of magnetic field. When $l^* = 6$, ΔT_{ad} is negligible because the magneto-induced strain is difficult to achieve the critical transformation strain. Under a larger l^*, the ΔT_{ad} increases with increasing l^*, and a critical value of l^* is seem to be observed in the inset of Fig. 7a. The impact of A^* on ΔT_{ad} is similar to the case of l^*, as shown in Fig. 7b. These results about the impact of the geometric dimension is in good agreement with the experimental [22] and simulated results [33]. The increase of A^* and l^* not only enhances ΔT_{ad}, but also reduces the critical magnetic driving force. In a word, the size of Terfenol-D should be more larger than the SMA, which is easier to induce MT and achieve a larger ΔT_{ad}. Optimizing the geometric dimension by increasing the length ratio and cross-sectional area ratios of Terfenol-D and MnCu is a sensible way to improve ΔT_{ad}.

3.2.4. Impact of ambient temperature

A higher ambient temperature will lead to a bigger critical phase transformation stress for MnCu SMA, which restricts the application of M-eCE cooling devices. Herein, the temperature-dependent M-eCE is investigated, as shown in Fig. 8. During the high temperature region (above the transition temperature), ΔT_{ad} decreases as the ambient temperature increases. The adjustments of applied magnetic field ($\mu_0 H$) and geometric dimension (A^* and l^*) could decrease the temperature sensitivity of ΔT_{ad} and widen the work temperature window of the M-eCE cooling system, which greatly promotes its commercial use. As shown in Fig. 8a, ΔT_{ad} for $A^* = 40$ and 80, $l^* = 26$, and $\mu_0 H = 0.19$ T is still higher than 10 K under 270 K. There is no obvious drop in ΔT_{ad} under high temperature. Because of the force balance for the M-eCE composite system, the magneto-induced strain (ε_2 in Eq. (16)) increases with A^* and l^*, which plays a role in reducing the critical magnetic field.

Similar to the mechanical load for eCE, the applied magnetic field also plays a positive role in ΔT_{ad}. The higher magnetostrictive strain caused by the bigger magnetic field would offer enough mechanical load to induce MT under a high temperature, thus leading to an appreciable ΔT_{ad}. The increase of magnetic field $\mu_0 H$, cross-sectional area ratios A^*, and length ratios l^* obviously enhances ΔT_{ad}, further widening the work temperature window to about 30 K. These efforts will make it possible to achieve room-temperature cooling without contact by using the M-eCE composite.

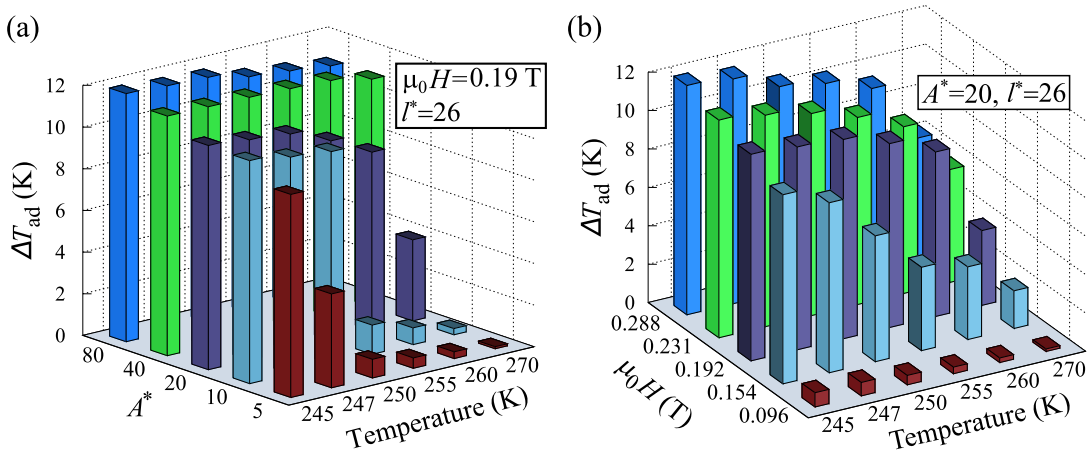

Fig. 8. The temperature dependence of adiabatic temperature change ΔT_{ad} under (a) various area ratios with $\mu_0 H = 0.19$ T and $l^* = 16$, and (b) various magnetic fields $\mu_0 H$ with $A^* = 20$ and $l^* = 26$.

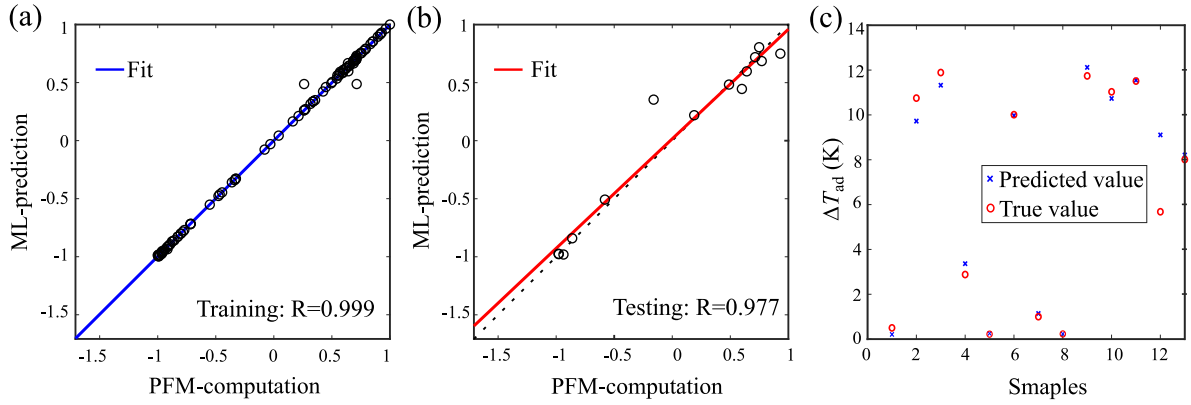

Fig. 9. The performance of ML prediction in the (a) training and (b) testing, and (c) comparison of the ML predicted values and true values of ΔT_{ad}. The true value of ΔT_{ad} signifies the phase-field calculated one.

3.3. Machine learning for M-eCE

ML is adopted to predict ΔT_{ad} by means of the database from phase-field simulation. Here R^2, root means square error ($RMSE$), and mean absolute error (MAE) are used to evaluate the performance of the ML neural network [79,82], i.e.,

$$R^2 = 1 - \frac{\sum_{i=1}^{m}(y_i - \hat{y}_i)^2}{\sum_{i=1}^{m}(y_i - \bar{y}_i)}, \tag{22}$$

$$RMSE = \sqrt{\frac{1}{m}\sum_{i=1}^{m}(y_i - \hat{y}_i)^2}, \tag{23}$$

$$MAE = \frac{1}{m}\sum_{i=1}^{m}|y_i - \hat{y}_i|, \tag{24}$$

where m is the number of samples, y_i is the true value of the sample, $\hat{y}_i$ is the predictive value, and $\bar{y}_i$ is the mean value. The value of R^2 is close to 1, which means that the error between the true value and predicted value is tiny, indicating that the ML model performs well. Fig. 9 shows the performance of ML in predicting ΔT_{ad}. $R^2 = 0.95$ shows ΔT_{ad} could be accurately predicted from the four characteristics. In addition, $RMSE$ and MAE are 0.134 and 0.038 for training set, and 0.238, and 0.141 for testing set, respectively. This indicates the small difference between the predicted and true values, as well as high accuracy of the ML prediction model. A correct ΔT_{ad} for a given magnetic field, length ratio, area ratio, and ambient temperature could be obtained through the ML model. Herein, the predicted value coincides well with the PFM simulated value, as shown in Fig. 9c. The configurations with larger ΔT_{ad} are found to own the characteristics of large A^* or l^*. Further, compared with the phase-field calculations for M-eCE, the time-saving ML model enhances computational efficiency by a factor of 10^4. ML saves a lot of computational costs and shortens the ΔT_{ad} prediction time from hours of phase-field calculation to seconds.

Furthermore, the optimization and parameter sensitivity analysis are performed, as shown in Fig. 10. Considering the influence of magnetic field, geometric dimension, and ambient temperature on M-eCE, a superior Pearson correlation coefficient (PCC) [83] can effectively measure the importance of the influence of the characteristic parameter X on the target value Y, i.e.,

$$PCC(X,Y) = \frac{\sum_{i=1}^{n}(X_i - \overline{X})(Y_i - \overline{Y})}{\sqrt{\sum_{i=1}^{n}(X_i - \overline{X})^2}\sqrt{\sum_{i=1}^{n}(Y_i - \overline{Y})^2}}, \tag{25}$$

where $\overline{X}$ and $\overline{Y}$ are the means of X and Y; n is the number of samples in the data set. The correlation between ΔT_{ad} (Y) and characteristic parameters, including magnetic field, geometric dimension and ambient temperature (X), is calculated using the PCC method, as shown in Fig. 10a. Larger PCC values indicated a more relevant correlation between the characteristic parameters and target parameter. The length ratio, area ratio, and magnetic field all play a positive role in ΔT_{ad}, especially for the magnetic field. The negative PCC values mean a hindering effect of the ambient temperature on the target parameter ΔT_{ad}.

Moreover, a variance-based sensitivity analysis [84] is conducted to identify the total effect on ΔT_{ad} for each characteristic parameters,

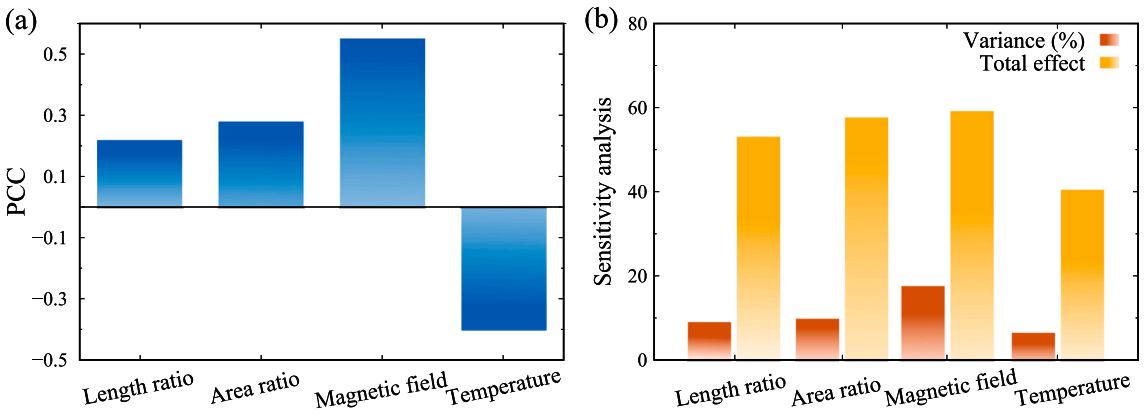

Fig. 10. The histograms of (a) Pearson correlation coefficient (PCC) and (b) sensitivity analysis between ΔT_{ad} and characteristic parameter inputs. The inputs of characteristic parameter include length ratio, area ratio, magnetic field, and temperature.

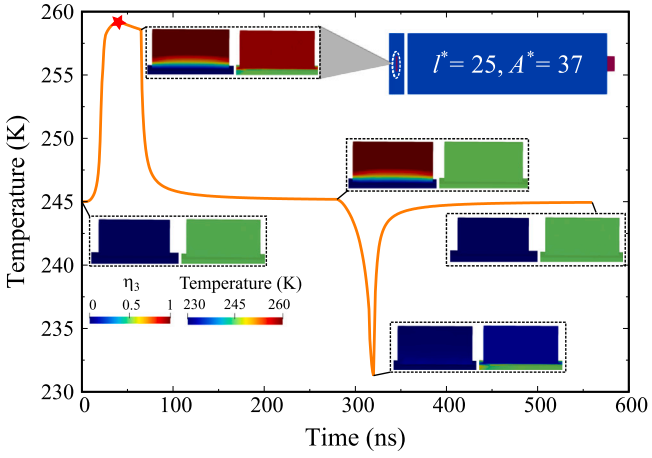

Fig. 11. The phase-field simulation of ML-optimization MEA-SMA composite with a combination of $A^* = 37$, $l^* = 25$, and $\mu_0 H = 0.384$ T. The yellow solid line represents the temperature change during the magneto-elastocaloric cooling cycle. The left side of the illustration shows the martensitic transformation distribution in SMA, where blue ($\eta_3 = 0$) represents austenite and red ($\eta_3 = 1$) represents the austenite phase. The right side shows the temperature distribution.

as shown in Fig. 10b. Obviously, there is a similar level of total effect as for the four characteristics from the results of PCC and sensitivity analysis. The contribution to ΔT_{ad} for length ratio and area ratio is equal, and the magnetic field is the most important to modulate ΔT_{ad}, which is similar to the PCC result. Based on the aforementioned analysis, ML is employed to optimize the multiferroic device and find the configuration with the ΔT_{ad}^{max}. In terms of the MEA-SMA composite size, ML optimizations show that $A^* = 37$, $l^* = 25$ and $\mu_0 H = 0.384$ T could achieve a large ΔT_{ad} (approx. 15 K) at an ambient temperature of 245 K. According to the ML optimizations, a phase-field simulation for a combination of $A^* = 37$, $l^* = 25$, and $\mu_0 H = 0.384$ T is performed, as shown in Fig. 11. The ΔT_{ad}^{max} by this PFM simulation is 14 K, which agrees well with the results from ML optimizations. The large ΔT_{ad} is attributed to the complete MT during SMA under the optimized MEA-SMA composite. This configuration further exhibits temperature insensitivity and magnetic-field insensitivity that a ΔT_{ad} of 11 K can still be obtained under a low magnetic field of 0.19 T and a high ambient temperature of 275 K. The performance enhancements of M-eCE indicate that ML could accelerate and optimize the design of M-eCE cooling devices with larger ΔT_{ad}.

4. Conclusions

In summary, we have proposed a non-isothermal PFM coupled with magnetostrictive constitutive model and a combination of PFM and ML to provide a quantitative simulation and understanding of recent experiments on the low-field induced M-eCE in the multiferroic MEA-SMA composite. In particular, to avoid the problematic calculation due to the non-differentiable energy barrier function across the transformation temperature, the austenite–martensite transition energy barrier in PFM is constructed as a smooth function of temperature by using the hyperbolic tangent function. It is shown that within this PFM framework, ferroelastic behavior in SMA, magnetostrictive behavior in MEA and M-eCE in MEA-SMA can be well reproduced. The maximum temperature rise/drop of SMA cuboid in the composite system during the rapid application and removal of the magnetic field can be well predicted by the proposed PFM, which are consistent with the experimental observations.

After examining the influence of magnetic field, geometric dimension including length ratio and area ratio, and ambient temperature on M-eCE, it is found that the magneto-induced strain in SMA plays a critical role in determining ΔT_{ad}, and manipulating magnetic field and geometric dimension can improve ΔT_{ad} and work temperature window. In detail, a large ΔT_{ad} of 10–14 K and a wide work temperature window from 245 to 275 K could be obtained under a low magnetic field of 0.15–0.38 T.

Furthermore, ML leveraging a database derived from phase-field simulations is performed to accelerate the prediction of M-eCE. ΔT_{ad} could be accurately predicted within $R^2 = 0.95$. ML significantly reduces computing costs and accelerates ΔT_{ad} prediction from hours of phase-field calculation to seconds. Along with the PCC and sensitivity analysis in ML, it is revealed that a combination of $A^* = 37$, $l^* = 25$, and $\mu_0 H = 0.384$ T by ML optimization could realize a large ΔT_{ad} around 14 K at an ambient temperature of 245 K. This configuration further exhibits temperature and magnetic-field insensitivity, which indicates the low-field M-eCE could be achieved by designing MEA-SMA composite based on PFM and ML. Compared to the multi-scale approach [33] and pure ML approach [70], the proposed combination of PFM and ML is easier to be extended to other multicaloric materials or cooling systems (e.g., electro-elastocaloric effect [20]), and provides a potential computational toolkit to unveil strategies for designing high-performance M-eC cooling devices.

CRediT authorship contribution statement

Wei Tang: Writing – original draft, Visualization, Investigation, Formal analysis, Data curation. **Shizheng Wen:** Writing – original draft, Investigation, Data curation, Conceptualization. **Huilong Hou:** Writing

– review & editing, Writing – original draft, Supervision, Resources, Investigation, Data curation, Conceptualization. **Qihua Gong:** Writing – review & editing, Writing – original draft, Supervision, Resources, Investigation, Data curation, Conceptualization. **Min Yi:** Writing – review & editing, Writing – original draft, Supervision, Resources, Project administration, Funding acquisition, Conceptualization. **Wanlin Guo:** Writing – review & editing, Supervision, Resources, Conceptualization.

Declaration of competing interest

The authors declare that they have no known competing financial interests or personal relationships that could have appeared to influence the work reported in this paper.

Data availability

Data will be made available on request.

Acknowledgments

The authors acknowledge the support from the National Natural Science Foundation of China (12272173, 12302134, 11902150), the Fundamental Research Funds for the Central Universities (NS2023054), the National Youth Talents Program, the Research Fund of State Key Laboratory of Mechanics and Control for Aerospace Structures, and a project Funded by the Priority Academic Program Development of Jiangsu Higher Education Institutions. This work is partially supported by High Performance Computing Platform of Nanjing University of Aeronautics and Astronautics. Simulations were also performed on Hefei advanced computing center.

Appendix. Finite-element implementation

Here, we use finite element method to solve the governing equations in Eqs. (12), (19), (20) and convert the strong forms into weak forms by introducing a test function. The degree of freedom is set as $u_1, u_2, u_3, \eta_1, \eta_2, \eta_3, T$, and the weak forms are formulated as

$$\begin{aligned}
0 &= \int_\Omega \sigma_{ij}\phi_{i,j}\mathrm{d}v - \int_{\partial\Omega}\sigma_{ij}n_j\phi_i\mathrm{d}s \\
0 &= \int_\Omega \left[\psi_i\left(\frac{\dot{\eta}_i}{L} + \frac{\partial f^{\mathrm{chem}}}{\partial \eta_i} + \frac{\partial f^{\mathrm{ela}}}{\partial \eta_i}\right) + \psi_{i,i}\beta\eta_{i,i}\right]\mathrm{d}v \\
&\quad - \int_{\partial\Omega}\psi_i\beta\eta_{i,i}n_i\mathrm{d}s \\
0 &= \int_\Omega \left[\vartheta\left(c_{\mathrm{v}}\dot{T} - Q\sum_{i=1}^{3}\dot{\eta}_i\right) + \vartheta_{,i}\alpha T_{,i}\right]\mathrm{d}v - \int_{\partial\Omega}\vartheta\alpha T_{,i}n_i\mathrm{d}s
\end{aligned} \tag{A.1}$$

where ϕ_i, ψ_i and ϑ are the test function for u_i, η_i and T, respectively. Note that the surface terms ($\sigma_{ij}n_j$ and $T_{,i}n_i$) in Eq. (A.1) represent the surface traction and heat flux boundary conditions.

By introducing the shape functions for independent variables and test functions, the discretized equations can be written as

$$\begin{aligned}
&u_i = N^I u_i^I \qquad \eta_i = N^I \eta_i{}^I \qquad \dot{\eta}_i = N^I \dot{\eta}_i{}^I \qquad T = N^I T^I \\
&\dot{T} = N^I \dot{T}^I \qquad \phi_i = N^I \phi_i^I \qquad \psi_i = N^I \psi_i{}^I \qquad \vartheta = N^I \vartheta^I
\end{aligned} \tag{A.2}$$

where I denotes the node number. N^I is the shape function. After the insertion of Eq. (A.2) into Eq. (A.1), the following elemental residuals can be obtained

$$\begin{aligned}
R^I_{u_i} &= \int_\Omega \sigma_{ij}N^I_{,j}\mathrm{d}v - \int_{\partial\Omega}N^I\sigma_{ij}n_j\mathrm{d}s \\
R^I_{\eta_i} &= \int_\Omega \left[N^I\left(\frac{1}{L}\dot{\eta}_i + \frac{\partial f^{\mathrm{ela}}}{\partial \eta_i} + \frac{\partial f^{\mathrm{chem}}}{\partial \eta_i}\right) + \beta\eta_{i,i}N^I_{,i}\right]\mathrm{d}v \\
&\quad - \int_{\partial\Omega}N^I\beta\eta_{i,i}n_i\mathrm{d}s \\
R^I_T &= \int_\Omega \left[N^I\left(c_{\mathrm{v}}\dot{T} - Q\sum_{i=1}^{3}\dot{\eta}_i\right) + N^I_{,i}\alpha T_{,i}\right]\mathrm{d}v - \int_{\partial\Omega}N^I\alpha T_{,i}n_i\mathrm{d}s.
\end{aligned} \tag{A.3}$$

With regard to the time dependence of the residuals, we use the implicit backward Euler method to realize the time discretization [62]. The residual equation for the current time step t_{n+1} is

$$\underline{\mathbf{R}}^I_{n+1} = \underline{\mathbf{R}}^I\left(\underline{\mathbf{d}}^J_{n+1}, \frac{\underline{\mathbf{d}}^J_{n+1} - \underline{\mathbf{d}}^J_n}{\Delta t}\right), \tag{A.4}$$

where $(\underline{\mathbf{d}}^J_{n+1} - \underline{\mathbf{d}}^J_n)/\Delta t = \underline{\dot{\mathbf{d}}}^J_{n+1}$ and Δt is time step. $\underline{\mathbf{d}}^J_{n+1}$ should be solved in this equation. For solving these non-linear equations, the Newton iteration scheme is performed at each time step. The corresponding iteration matrix is

$$\underline{\mathbf{S}}^{IJ} = \underline{\mathbf{K}}^{IJ} + \frac{1}{\Delta t}\underline{\mathbf{D}}^{IJ}, \tag{A.5}$$

where $\underline{\mathbf{K}}^{IJ}$ is the stiffness matrix and $\underline{\mathbf{D}}^{IJ}$ is the damping matrix. The PFM is numerically implemented in open source Multiphysics Object Oriented Simulation Environment (MOOSE) [81].

References

[1] Bonnot E, Romero R, Mañosa L, Vives E, Planes A. Elastocaloric effect associated with the martensitic transition in shape-memory alloys. Phys Rev Lett 2008;100(12):125901. http://dx.doi.org/10.1103/PhysRevLett.100.125901.
[2] Tušek J, Engelbrecht K, Mikkelsen LP, Pryds N. Elastocaloric effect of Ni-Ti wire for application in a cooling device. J Appl Phys 2015;117(12):124901. http://dx.doi.org/10.1063/1.4913878.
[3] Chen J, Liu B, Xing L, Liu W, Lei L, Fang G. Toward tunable mechanical behavior and enhanced elastocaloric effect in NiTi alloy by gradient structure. Acta Mater 2022;226:117609. http://dx.doi.org/10.1016/j.actamat.2021.117609.
[4] Franco V, Blázquez J, Ipus J, Law J, Moreno-Ramírez L, Conde A. Magnetocaloric effect: From materials research to refrigeration devices. Prog Mater Sci 2018;93:112–232. http://dx.doi.org/10.1016/j.pmatsci.2017.10.005.
[5] He W, Yin Y, Gong Q, Evans RFL, Gutfleisch O, Xu B-X, Yi M, Guo W. Giant magnetocaloric effect in magnets down to the monolayer limit. Small 2023;19(36):2300333. http://dx.doi.org/10.1002/smll.202300333.
[6] Scott J. Electrocaloric materials. Annu Rev Mater Res 2011;41:229–40. http://dx.doi.org/10.1146/annurev-matsci-062910-100341.
[7] Hou X, Li X, Zhang J, Bag SP, Li H, Wang J. Effect of grain size on the electrocaloric properties of polycrystalline ferroelectrics. Phys Rev A 2021;15(5):054019. http://dx.doi.org/10.1103/PhysRevApplied.15.054019.
[8] Greco A, Aprea C, Maiorino A, Masselli C. A review of the state of the art of solid-state caloric cooling processes at room-temperature before 2019. Int J Refrig 2019;106:66–88. http://dx.doi.org/10.1016/j.ijrefrig.2019.06.034.
[9] Wang Y, Liu Y, Xu S, Zhou G, Yu J, Qian S. Towards practical elastocaloric cooling. Commun Eng 2023;2(1):79.
[10] Chauhan A, Patel S, Vaish R, Bowen CR. A review and analysis of the elastocaloric effect for solid-state refrigeration devices: Challenges and opportunities. MRS Energy Sustain 2015;2. http://dx.doi.org/10.1557/mre.2015.17.
[11] Li X, Hua P, Sun Q. Continuous and efficient elastocaloric air cooling by coil-bending. Nature Commun 2023;14(1):7982.
[12] Chen Y, Wang Y, Sun W, Qian S, Liu J. A compact elastocaloric refrigerator. Innovation 2022;3(2):100205. http://dx.doi.org/10.1016/j.xinn.2022.100205.
[13] Hou H, Simsek E, Stasak D, Al Hasan N, Qian S, Ott R, Cui J, Takeuchi I. Elastocaloric cooling of additive manufactured shape memory alloys with large latent heat. J Phys D: Appl Phys 2017;50(40):404001.
[14] Hou H, Simsek E, Ma T, Johnson NS, Qian S, Cissé C, Stasak D, Hasan NA, Zhou L, Hwang Y, Radermacher R, Levitas VI, Kramer MJ, Zaeem MA, Stebner AP, Ott RT, Cui J, Takeuchi I. Fatigue-resistant high-performance elastocaloric materials made by additive manufacturing. Science 2019;366(6469):1116–21. http://dx.doi.org/10.1126/science.aax7616.
[15] Wu Y, Ertekin E, Sehitoglu H. Elastocaloric cooling capacity of shape memory alloys – role of deformation temperatures, mechanical cycling, stress hysteresis and inhomogeneity of transformation. Acta Mater 2017;135:158–76. http://dx.doi.org/10.1016/j.actamat.2017.06.012.
[16] Qian S, Geng Y, Wang Y, Pillsbury TE, Hada Y, Yamaguchi Y, Fujimoto K, Hwang Y, Radermacher R, Cui J, et al. Elastocaloric effect in CuAlZn and CuAlMn shape memory alloys under compression. Phil Trans R Soc A 2016;374(2074):20150309. http://dx.doi.org/10.1098/rsta.2015.0309.
[17] Tušek J, Engelbrecht K, Mañosa L, Vives E, Pryds N. Understanding the thermodynamic properties of the elastocaloric effect through experimentation and modelling. Shape Memory Superelast 2016;2(4):317–29. http://dx.doi.org/10.1007/s40830-016-0094-8.
[18] Xu S, Huang H-Y, Xie J, Takekawa S, Xu X, Omori T, Kainuma R. Giant elastocaloric effect covering wide temperature range in columnar-grained $Cu_{71.5}Al_{17.5}Mn_{11}$ shape memory alloy. APL Mater 2016;4(10):106106. http://dx.doi.org/10.1063/1.4964621.

[19] Silva DJ, Ventura J, Araujo JP. Caloric devices: A review on numerical modeling and optimization strategies. Int J Energy Res 2021;45(13):18498–539. http://dx.doi.org/10.1002/er.7023.

[20] Hou H, Qian S, Takeuchi I. Materials, physics and systems for multicaloric cooling. Nat Rev Mater 2022;1–20. http://dx.doi.org/10.1038/s41578-022-00428-x.

[21] Qian S, Catalini D, Muehlbauer J, Liu B, Mevada H, Hou H, Hwang Y, Radermacher R, Takeuchi I. High-performance multimode elastocaloric cooling system. Science 2023;380(6646):722–7. http://dx.doi.org/10.1126/science.adg7043.

[22] Hou H, Finkel P, Staruch M, Cui J, Takeuchi I. Ultra-low-field magneto-elastocaloric cooling in a multiferroic composite device. Nature Commun 2018;9(1):1–8. http://dx.doi.org/10.1038/s41467-018-06626-y.

[23] Shen Y, Wei Z, Sun W, Zhang Y, Liu E, Liu J. Large elastocaloric effect in directionally solidified all-d-metal Heusler metamagnetic shape memory alloys. Acta Mater 2020;188:677–85. http://dx.doi.org/10.1016/j.actamat.2020.02.045.

[24] Amirov AA, Gottschall T, Chirkova AM, Aliev AM, Baranov NV, Skokov KP, Gutfleisch O. Electric-field manipulation of the magnetocaloric effect in a $Fe_{49}Rh_{51}$/PZT composite. J Phys D: Appl Phys 2021;54(50):505002. http://dx.doi.org/10.1088/1361-6463/ac25ae.

[25] Liu Y, Phillips LC, Mattana R, Bibes M, Barthélémy A, Dkhil B. Large reversible caloric effect in FeRh thin films via a dual-stimulus multicaloric cycle. Nature Commun 2016;7(1):1–6. http://dx.doi.org/10.1038/ncomms11614.

[26] Niu L, Shi Y, Gao Y. Effect of magnetic-field orientation on dual-peak phenomenon of magnetoelectric coupling in Ni/PZT/Terfenol-D composites. AIP Adv 2019;9(4). http://dx.doi.org/10.1063/1.5084299.

[27] Liang X, Zhang C, Bai J, Gu J, Zhang Y, Esling C, Zhao X, Zuo L. Manipulation of magnetocaloric and elastocaloric effects in Ni–Mn–In alloys by lattice volume and magnetic variation: Effect of Co and Fe co-doping. J Mater Sci Technol 2024;172:156–65.

[28] Li B, Liu Z, Li D, Feng Z, Zhu J, Zhong H, Li S. Large reversible multicaloric effects over a broad refrigeration temperature range in Co and B co-doped Ni–Mn–Ti alloys. Mater Sci Eng A 2024;146260.

[29] Zhang Q, Chen J, Fang G. From mechanical behavior and elastocaloric effect to microscopic mechanisms of gradient-structured NiTi alloy: A phase-field study. Int J Plast 2023;171:103809. http://dx.doi.org/10.1016/j.ijplas.2023.103809.

[30] Liang C, Yin Y, Wang W, Yi M. A thermodynamically consistent non-isothermal phase-field model for selective laser sintering. Int J Mech Sci 2023;259:108602. http://dx.doi.org/10.1016/j.ijmecsci.2023.108602.

[31] Xu B, Xiong J, Yu C, Wang C, Wang Q, Kang G. Improved elastocaloric effect of NiTi shape memory alloys via microstructure engineering: A phase field simulation. Int J Mech Sci 2022;222:107256. http://dx.doi.org/10.1016/j.ijmecsci.2022.107256.

[32] Xu T, Wang C, Zhu Y, Wang Y, Yan Y, Wang J, Shimada T, Kitamura T. Efficient phase-field simulation for linear superelastic NiTi alloys under temperature gradients. Int J Mech Sci 2023;259:108592. http://dx.doi.org/10.1016/j.ijmecsci.2023.108592.

[33] Yu C, Kang G. A multiscale magneto-thermo-mechanically coupled model for ultra-low-field induced magneto-elastocaloric effect in magnetostrictive-shape memory alloy composite system. Internat J Engrg Sci 2021;168:103539. http://dx.doi.org/10.1016/j.ijengsci.2021.103539.

[34] Bachmann N, Fitger A, Unmüß ig S, Bach D, Schäfer-Welsen O, Koch T, Bartholomé K. Phenomenological model for first-order elastocaloric materials. Int J Refrig 2022;136:245–53. http://dx.doi.org/10.1016/j.ijrefrig.2022.01.009.

[35] Zhang Y, Kang G, Miao H, Yu C. Cyclic degeneration of elastocaloric effect for NiTi shape memory alloy: Experimental observation and constitutive model. Int J Solids Struct 2022;248:111638. http://dx.doi.org/10.1016/j.ijsolstr.2022.111638.

[36] Tanaka K. A thermomechanical sketch of shape memory effect: one-dimensional tensile behavior. Res Mech 1986;18(3):251–63.

[37] Tušek J, Engelbrecht K, Millán-Solsona R, Mañosa L, Vives E, Mikkelsen LP, Pryds N. The elastocaloric effect: a way to cool efficiently. Adv Energy Mater 2015;5(13):1500361. http://dx.doi.org/10.1002/aenm.201500361.

[38] Cheng S, Xiao Y, Li X, Lin H, Hua P, Sheng L. Continuous rotating bending NiTi sheets for elastocaloric cooling: Model and experiments. Int J Refrig 2023;147:39–47. http://dx.doi.org/10.1016/j.ijrefrig.2022.11.020.

[39] Zhang Y, Yu C, Di Song, Zhu Y, Kan Q, Kang G. Solid-state cooling with high elastocaloric strength and low driving force via NiTi shape memory alloy helical springs: Experiment and theoretical model. Mech Mater 2023;178:104575. http://dx.doi.org/10.1016/j.mechmat.2023.104575.

[40] Qian S, Ling J, Hwang Y, Radermacher R, Takeuchi I. Thermodynamics cycle analysis and numerical modeling of thermoelastic cooling systems. Int J Refrig 2015;56:65–80. http://dx.doi.org/10.1016/j.ijrefrig.2015.04.001.

[41] Qian S, Yuan L, Yu J, Yan G. The mechanism of ΔT variation in coupled heat transfer and phase transformation for elastocaloric materials and its application in materials characterization. Appl Phys Lett 2017;111(22):223902. http://dx.doi.org/10.1063/1.5001971.

[42] Qian S, Yuan L, Yu J, Yan G. Numerical modeling of an active elastocaloric regenerator refrigerator with phase transformation kinetics and the matching principle for materials selection. Energy 2017;141:744–56. http://dx.doi.org/10.1016/j.energy.2017.09.116.

[43] Yu C, Chen T, Yin H, Kang G, Fang D. Modeling the anisotropic elastocaloric effect of textured NiMnGa ferromagnetic shape memory alloys. Int J Solids Struct 2020;191:509–28. http://dx.doi.org/10.1016/j.ijsolstr.2019.12.020.

[44] Zhou T, Kang G, Yin H, Yu C. Modeling the two-way shape memory and elastocaloric effects of bamboo-grained oligocrystalline shape memory alloy microwire. Acta Mater 2020;198:10–24. http://dx.doi.org/10.1016/j.actamat.2020.07.057.

[45] Xu B, Yu C, Wang C, Kan Q, Wang Q, Kang G. Effect of pore on the deformation behaviors of NiTi shape memory alloys: A crystal-plasticity-based phase field modeling. Int J Plast 2024;175:103931. http://dx.doi.org/10.1016/j.ijplas.2024.103931.

[46] Chen L-Q. Phase-field models for microstructure evolution. Annu Rev Mater Sci 2002;32(1):113–40. http://dx.doi.org/10.1146/annurev.matsci.32.112001.132041.

[47] Levitas VI, Roy AM. Multiphase phase field theory for temperature-and stress-induced phase transformations. Phys Rev B 2015;91(17):174109. http://dx.doi.org/10.1103/PhysRevB.91.174109.

[48] Cui S, Wan J, Zuo X, Chen N, Zhang J, Rong Y. Three-dimensional, non-isothermal phase-field modeling of thermally and stress-induced martensitic transformations in shape memory alloys. Int J Solids Struct 2017;109:1–11. http://dx.doi.org/10.1016/j.ijsolstr.2017.01.001.

[49] Luo H, Tang W, Gong Q, Yi M. Giant enhancement of elastocaloric effect by introducing microstructural holes. J Alloys Compd 2023;932:167636. http://dx.doi.org/10.1016/j.jallcom.2022.167636.

[50] Cissé C, Zaeem MA. On the elastocaloric effect in CuAlBe shape memory alloys: A quantitative phase-field modeling approach. Comput Mater Sci 2020;183:109808. http://dx.doi.org/10.1016/j.commatsci.2020.109808.

[51] Xu B, Kang G. Phase field simulation on the super-elasticity, elastocaloric and shape memory effect of geometrically graded nano-polycrystalline NiTi shape memory alloys. Int J Mech Sci 2021;201:106462. http://dx.doi.org/10.1016/j.ijmecsci.2021.106462.

[52] Xu B, Wang C, Wang Q, Yu C, Kan Q, Kang G. Enhancing elastocaloric effect of NiTi alloy by concentration-gradient engineering. Int J Mech Sci 2023;246:108140. http://dx.doi.org/10.1016/j.ijmecsci.2023.108140.

[53] Zhang Y, Yu C, Zhu Y, Kan Q, Kang G. Thermo-mechanically coupled deformation of pseudoelastic NiTi SMA helical spring. Int J Mech Sci 2022;236:107767. http://dx.doi.org/10.1016/j.ijmecsci.2022.107767.

[54] Kan Q, Zhang Y, Shi W, Xu Y, Yu C, Kang G. Functional fatigue of superelasticity and elastocaloric effect for NiTi springs. Int J Mech Sci 2024;265:108889. http://dx.doi.org/10.1016/j.ijmecsci.2023.108889.

[55] Wan Y, Fang D, Hwang KC. Non-linear constitutive relations for magnetostrictive materials. Int J Non-Linear Mech 2003;38(7):1053–65. http://dx.doi.org/10.1016/S0020-7462(02)00052-5.

[56] Jin K, Kou Y, Zheng X. A nonlinear magneto-thermo-elastic coupled hysteretic constitutive model for magnetostrictive alloys. J Magn Magn Mater 2012;324(12):1954–61. http://dx.doi.org/10.1016/j.jmmm.2012.01.028.

[57] Hu CC, Zhang Z, Yang TN, Shi YG, Cheng XX, Ni JJ, Hao JG, Rao WF, Chen LQ. Phase field simulation of grain size effects on the phase coexistence and magnetostrictive behavior near the ferromagnetic morphotropic phase boundary. Appl Phys Lett 2019;115(16). http://dx.doi.org/10.1063/1.5118927.

[58] Zhan YS, hong Lin C. A constitutive model of coupled magneto-thermo-mechanical hysteresis behavior for giant magnetostrictive materials. Mech Mater 2020;148:103477. http://dx.doi.org/10.1016/J.MECHMAT.2020.103477.

[59] Zhang J, Chen L. Phase-field microelasticity theory and micromagnetic simulations of domain structures in giant magnetostrictive materials. Acta Mater 2005;53(9):2845–55. http://dx.doi.org/10.1016/j.actamat.2005.03.002.

[60] Hu C-C, Yang T-N, Huang H-B, Hu J-M, Wang J-J, Shi Y-G, Shi D-N, Chen L-Q. Phase-field simulation of domain structures and magnetostrictive response in $Tb_{1-x}Dy_xFe_2$ alloys near morphotropic phase boundary. Appl Phys Lett 2016;108(14):141908. http://dx.doi.org/10.1063/1.4945684.

[61] Yi M, Xu B-X. A real-space and constraint-free phase field model for the microstructure of ferromagnetic shape memory alloys. Int J Fract 2016;202(2):179–94. http://dx.doi.org/10.1007/s10704-016-0152-4.

[62] Yi M, Xu B-X. A constraint-free phase field model for ferromagnetic domain evolution. Proc R Soc Lond Ser A Math Phys Eng Sci 2014;470(2171):20140517. http://dx.doi.org/10.1098/rspa.2014.0517.

[63] Zhang Y, Kang G, Miao H, Yu C. Semi-analytical and numerical models for magnetic field induced magneto-elastocaloric cooling in the multiferroic composite system. Compos Struct 2022;289:115409. http://dx.doi.org/10.1016/j.compstruct.2022.115409.

[64] Dong Y, Zhu Y, Wu F, Yu C. A dual-scale elasto-viscoplastic constitutive model of metallic materials to describe thermo-mechanically coupled monotonic and cyclic deformations. Int J Mech Sci 2022;224:107332. http://dx.doi.org/10.1016/j.ijmecsci.2022.107332.

[65] Yu C, Zhou T, Kan Q, Kang G, Fang D. A two-scale thermo-mechanically coupled model for anomalous martensite transformation and elastocaloric switching effect of shape memory alloy. J Mech Phys Solids 2022;164:104893. http://dx.doi.org/10.1016/j.jmps.2022.104893.

[66] Dornisch W, Schrade D, Xu B-X, Keip M-A, Müller R. Coupled phase field simulations of ferroelectric and ferromagnetic layers in multiferroic heterostructures. Arch Appl Mech 2018;89:1031–56. http://dx.doi.org/10.1007/s00419-018-1480-9.

[67] Zhang Y, Xu X. Machine learning the magnetocaloric effect in manganites from compositions and structural parameters. AIP Adv 2020;10(3):035220.

[68] Zhang Y, Xu X. Machine learning the magnetocaloric effect in manganites from lattice parameters. Appl Phys A 2020;126(5):341.

[69] Yuan R, Liu Z, Xu Y, Yin R, He J, Bai Y, Zhou Y, Li J, Xue D, Lookman T. Optimizing electrocaloric effect in barium titanate-based room temperature ferroelectrics: Combining Landau theory, machine learning and synthesis. Acta Mater 2022;235:118054.

[70] Zhao X-P, Huang H-Y, Wen C, Su Y-J, Qian P. Accelerating the development of multi-component Cu-Al-based shape memory alloys with high elastocaloric property by machine learning. Comput Mater Sci 2020;176:109521.

[71] Tian X, Zhao Q, Zhang K, Li H, Han B, Shi D, Zhou L, Ma T, Wang C, Wen Q, et al. Accelerated design for elastocaloric performance in NiTi-based alloys through machine learning. J Appl Phys 2022;131(1):015104. http://dx.doi.org/10.1063/5.0068290.

[72] Ding L, Zhou Y, Xu Y, Dang P, Ding X, Sun J, Lookman T, Xue D. Learning from superelasticity data to search for Ti-Ni alloys with large elastocaloric effect. Acta Mater 2021;218:117200.

[73] Shimizu K, Okumura Y, Kubo H. Crystallographic and morphological studies on the FCC to FCT transformation in Mn–Cu alloys. Trans. Japan Inst. Metals 1982;23(2):53–9. http://dx.doi.org/10.2320/matertrans1960.23.53.

[74] Malik A, Amberg G, Borgenstam A, Agren J. Effect of external loading on the martensitic transformation-a phase field study. Acta Mater 2013;61(20):7868–80. http://dx.doi.org/10.1016/j.actamat.2013.09.025.

[75] Mañosa L, Planes A. Materials with giant mechanocaloric effects: cooling by strength. Adv Mater 2017;29(11):1603607. http://dx.doi.org/10.1002/adma.201603607.

[76] De Melo CS, Randeria M, Engelbrecht JR. Crossover from BCS to Bose superconductivity: Transition temperature and time-dependent Ginzburg–Landau theory. Phys Rev Lett 1993;71(19):3202. http://dx.doi.org/10.1103/physrevlett.71.3202.

[77] Albadr MA, Tiun S, Ayob M, Al-Dhief F. Genetic algorithm based on natural selection theory for optimization problems. Symmetry 2020;12(11):1758.

[78] Santosh S, Sampath V, Mouliswar R. Hot deformation characteristics of NiTiV shape memory alloy and modeling using constitutive equations and artificial neural networks. J Alloys Compd 2022;901:163451. http://dx.doi.org/10.1016/j.jallcom.2021.163451.

[79] Wen S, Dang C, Liu X. A machine learning strategy for modeling and optimal design of near-field radiative heat transfer. Appl Phys Lett 2022;121(7). http://dx.doi.org/10.1063/5.0103363.

[80] Zhou HM, Li MH, Li XH, Zhang DG. An analytical and explicit multi-field coupled nonlinear constitutive model for Terfenol-D giant magnetostrictive material. Smart Mater Struct 2016;25(8). http://dx.doi.org/10.1088/0964-1726/25/8/085036.

[81] Tonks MR, Gaston D, Millett PC, Andrs D, Talbot P. An object-oriented finite element framework for multiphysics phase field simulations. Comput Mater Sci 2012;51(1):20–9. http://dx.doi.org/10.1016/j.commatsci.2011.07.028.

[82] Yi M, Xue M, Cong P, Song Y, Zhang H, Wang L, Zhou L, Li Y, Guo W. Machine learning for predicting fatigue properties of additively manufactured materials. Chin J Aeronaut 2024;37(4):1–22. http://dx.doi.org/10.1016/j.cja.2023.11.001.

[83] Lian Z, Li M, Lu W. Fatigue life prediction of aluminum alloy via knowledge-based machine learning. Int J Fatigue 2022;157:106716.

[84] Kennedy M, Petropoulos G. The Gaussian Emulation Machine for Sensitivity Analysis. In: Petropoulos GP, Srivastava PK, editors. Sensitivity analysis in earth observation modelling. Elsevier; 2017, p. 341–61, Ch. 17.